PNAS RESEARCH ARTICLE | NEUROSCIENCE OPEN ACCESS

Human cone elongation responses can be explained by photoactivated cone opsin and membrane swelling and osmotic response to phosphate produced by RGS9-catalyzed GTPase

Vimal Prabhu Pandiyan[a], Phuong T. Nguyen[b], Edward N. Pugh Jr.[b,c,1], and Ramkumar Sabesan[a,1]

Edited by Theodore Wensel, Baylor College of Medicine, Houston, TX; received February 10, 2022; accepted August 5, 2022 by Editorial Board Member Jeremy Nathans

Human cone outer segment (COS) length changes in response to stimuli bleaching up to 99% of L- and M-cone opsins were measured with high resolution, phase-resolved optical coherence tomography (OCT). Responses comprised a fast phase (~5 ms), during which COSs shrink, and two slower phases (1.5 s), during which COSs elongate. The slower components saturated in amplitude (~425 nm) and initial rate (~3 nm ms^{-1}) and are well described over the 200-fold bleaching range as the sum of two exponentially rising functions with time constants of 80 to 90 ms (component 1) and 1,000 to 1,250 ms (component 2). Measurements with adaptive optics reflection densitometry revealed component 2 to be linearly related to cone pigment bleaching, and the hypothesis is proposed that it arises from cone opsin and disk membrane swelling triggered by isomerization and rate-limited by chromophore hydrolysis and its reduction to membrane-localized all-trans retinol. The light sensitivity and kinetics of component 1 suggested that the underlying mechanism is an osmotic response to an amplified soluble by-product of phototransduction. The hypotheses that component 1 corresponds to G-protein subunits dissociating from the membrane, metabolites of cyclic guanosine monophosphate (cGMP) hydrolysis, or by-products of activated guanylate cyclase are rejected, while the hypothesis that it corresponds to phosphate produced by regulator of G-protein signaling 9 (RGS9)-catalyzed hydrolysis of guanosine triphosphate (GTP) in G protein–phosphodiesterase complexes was found to be consistent with the results. These results provide a basis for the assessment with optoretinography of phototransduction in individual cone photoreceptors in health and during disease progression and therapeutic interventions.

cone photoreceptors | photosensitivity | opsin bleaching | optical coherence tomography | optoretinogram

Significance

Optical coherence tomography has established that human cone photoreceptor outer segments elongate in response to stimuli bleaching large fractions of their visual pigment. Elongation responses are completely described over their 200-fold bleaching range as the sum of two exponentially rising components differing 13-fold in time constants and 4-fold in light sensitivity. Bleaching measurements of individual cones with adaptive optics scanning laser ophthalmoscopy (SLO) suggest that component 2 arises from cone opsin and disk membrane swelling triggered by photoactivation. Application of a model of phototransduction suggests that component 1 corresponds to free phosphate generated by regulator of G-protein signaling 9 (RGS9)-catalyzed hydrolysis of guanosine triphosphate (GTP) in the α-subunit of G protein complexed with phosphodiesterase.

Cone photoreceptors initiate the high-acuity daytime vision of healthy humans. The loss of central retinal cone function, as occurs in age-related macular degeneration, is personally devastating and medically extremely costly (1, 2). Over the past 25 y, thanks to the development of optical coherence tomography (OCT) (3, 4) and the application of adaptive optics (AO) to retinoscopy (5–7), there have been enormous advances in imaging the cone mosaic at single-cell resolution in the living eye. Very recently, nanometer-scale measurements of the optical path length (OPL) of rod and cone outer segments (COSs) have made it possible to "optoretinographically" quantify light-driven length changes of individual human COSs (8–14), affording a cell by cell assessment of normal cone function and of dysfunction in disease states (15), with great potential value for evaluating therapeutic interventions. Other than the dependence of rod outer segment (ROS) elongation on the G protein transducin (16), no specific molecular mechanisms of light-driven outer segment elongation, however, have been identified.

In this investigation, hypotheses for the molecular mechanisms of human COS elongation are proposed and tested. The kinetics and bleaching sensitivity of the COS responses were measured in response to brief light stimuli ranging 200-fold in intensity, up to and including intensities that bleach the entire complement of cone opsin. The bleach-level dependence and kinetics strongly constrain hypotheses that could underlie COS elongation, rejecting G-protein subunits dissociated from the membrane, by-products of phosphodiesterase-catalyzed cyclic guanosine monophosphate (cGMP) hydrolysis or of guanylate cyclase synthesis of cGMP, and changes in ionic concentrations. Application of a model of cone phototransduction appropriate for the extreme bleaching levels involved supports the hypotheses that COS elongation is partly driven by the osmotic response to free phosphate (P_i) produced by the regulator of G-protein signaling 9 (RGS9)-catalyzed hydrolysis of guanosine triphosphate (GTP) in the $G_{tc}\alpha$–phosphodiesterase (PDE) complex and partly driven by bleaching-induced swelling of cone opsin (17) and disk membrane expansion attendant chromophore hydrolysis and its reduction to all-trans retinol (at-ROL) (18).

Author contributions: E.N.P. and R.S. designed research; V.P.P. and R.S. performed research; P.T.N. contributed new reagents/analytic tools; V.P.P., E.N.P., and R.S. analyzed data; and E.N.P. and R.S. wrote the paper.

The authors declare no competing interest.

This article is a PNAS Direct Submission. T.W. is a guest editor invited by the Editorial Board.

[1]To whom correspondence may be addressed. Email: enpugh@ucdavis.edu or rsabesan@uw.edu.

This article contains supporting information online at http://www.pnas.org/lookup/suppl/doi:10.1073/pnas.2202485119/-/DCSupplemental.

Published September 19, 2022.

Results

COS Elongation Exhibits Rate and Amplitude Saturation in Response to Increasingly Intense Stimulation. COS elongation responses to light exposures that bleach large fractions of cone pigment exhibit two distinct forms of saturation: of their initial rate and of their amplitude (Fig. 1). Rate saturation is seen in the rising phase of the elongation. Thus, responses to stimuli whose retinal energy density exceeds ~10^7 Troland seconds (Td s) (4×10^9 λ_{max}-equivalent photons μm^{-2} at the retinal surface) rise initially along a common maximal slope of ~4 nm ms^{-1}, while amplitude saturation is manifest as a coincidence of the responses to these stimuli (Fig. 1*B*, black traces; cf *SI Appendix*, Fig. S1). The saturated traces can be precisely described as comprising two exponentially rising components that differ by more than 10-fold in their time constants (Fig. 1 *C* and *D*).

COS Elongation Responses to Bleaching Stimuli Spanning an ~200-fold Range of Intensities Are Well Characterized as Sums of the Same Two Components. To determine whether the entire family of COS elongation responses can be described as combinations of the same underlying components, we fitted each of the traces in a response family with a weighted sum of the two exponentially rising functions extracted from the saturating response (Fig. 2). This decomposition recapitulated the response family (Fig. 2*A*, cyan traces), with little systematic deviation (Fig. 2*B*). Subtracting one or the other fitted component from the original traces provided a means of visualizing the individual components, hereafter identified as component 1 (Fig. 2*C*, red) and component 2 (Fig. 2*C*, blue). The trace by trace fitting analysis yielded one amplitude scaling factor for each component for each stimulus intensity; plotting the two sets of scale factors against the retinal energy density of the stimuli revealed the production of component 1 to be three- to sixfold more sensitive to light than that of component 2 (Fig. 2*D*). Another striking difference between the two components is their small signal gain (units: fractional amplitude $second^{-1}$); the ratio of gains of component 1 to component 2 was 63 for subject 1, while for subject 2, the ratio was 54-fold.

In summary, over the 200-fold range of intensities that cause human COS elongation, it can be characterized as arising from two components differing 13-fold in their maximal rates (Fig. 2*C*), 3- to 6-fold in light sensitivity (Fig. 2*D*), and more than 50-fold in small signal gain.

The Photosensitivity of Component 2 Is Consistent with Being a Stoichiometric By-Product of Cone Pigment Bleaching. The very high–intensity dependence of component 2 is comparable with that of cone pigment bleaching measured in prior investigations with retinal reflection densitometry and psychophysical methods (19–24) (Fig. 2*D*), suggesting that the molecular mechanism underlying this component of the COS elongation response is stoichiometrically related to bleaching. To examine this hypothesis, we measured the photosensitivity of cone pigment bleaching with AO serial scanning reflection densitometry, a method that obviates contamination from rods (25), and compared these measurements with the photosensitivity of component 2 (*SI Appendix*, Fig. S2). To address discrepancies between our photosensitivity measurements and those of prior studies, we formalized the hypothesis that the photon energy density at the retinal surface (Q_{retina}) and that ($Q_{COS,\ inc}$) incident at the COS waveguide entrance (i.e., at the COS basal disks after propagation through the cone inner segment [CIS]) are related by a product of quantifiable scaling factors: that is,

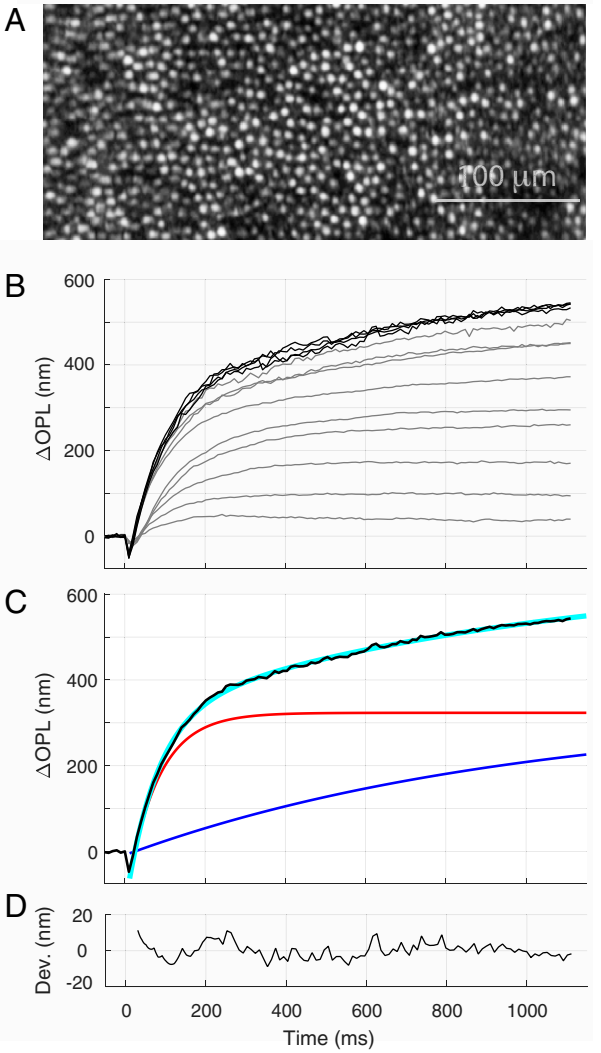

Fig. 1. Light exposures that bleach large fractions of cone opsins generate rate- and amplitude-saturated COS elongation responses. (*A*) OCT en face image of a portion of the temporal retina of subject 1 at 7° eccentricity that was stimulated with brief bleaching exposures. Each light dot corresponds to a single cone. Changes in COS OPL (ΔOPL) were measured with OCT from 247 cones at 30 Hz and averaged. (*B*) Kinetics of average ΔOPL in response to light exposures ranging ~200-fold in retinal energy density; the most intense stimulus is estimated to isomerize (bleach) more than 90% of the L- and M-cone opsins (cf *SI Appendix*, Fig. S2). The responses to the four most intense stimuli are nearly identical and are plotted as black traces, while the responses to lower-intensity stimuli are plotted in gray. Each trace is an average of two to four repetitions, with 4 to 5 min of dark adaptation in between stimuli. (Additional experiments with longer recording durations showed that the slope of the saturating traces at 2 s was effectively zero and also further quantified rate saturation [*SI Appendix*, Fig. S1 and section 1].) (*C*) The average (black trace) of the four rate- and amplitude-saturated traces of *B* was fitted by least squares (MATLAB; lsqcurvefit) with the sum (cyan) of two rising exponential functions. The time constants and asymptotic amplitudes of the two functions are τ_1 = 78 ms, $\Delta OPL_1(\infty)$ = 323 nm (red) and τ_2 = 980 ms, $\Delta OPL_2(\infty)$ = 332 nm (blue), respectively. (*D*) Residual deviations of the data trace in *C* from the fitted curve plotted on an expanded ordinate scale; the root mean square (RMS) deviation of the data (black) trace from the fitted curve (cyan) in *C* is 3.9 nm. For similar saturated data from subject 2, the parameters describing the two components were τ_1 = 92 ms, $\Delta OPL_1(\infty)$ = 350 nm and τ_2 = 1,200 ms, $\Delta OPL_2(\infty)$ = 238 nm, respectively, and the RMS deviation was 4.6 nm. (Changes in the physical length of the COS are obtained by the relation $\Delta L_{COS} = \Delta OPL / n_{COS}$, where n_{COS} = 1.41 is the refractive index of the COS.)

$$Q_{COS,inc} = Q_{retina} f_{WFA} f_{SCI} f_{CIS2COS}. \quad [1]$$

Here, $0 < f_{WFA} < 1$ represents potential loss due to wavefront aberration (26), $0 < f_{SCI} < 1$ represents the cone

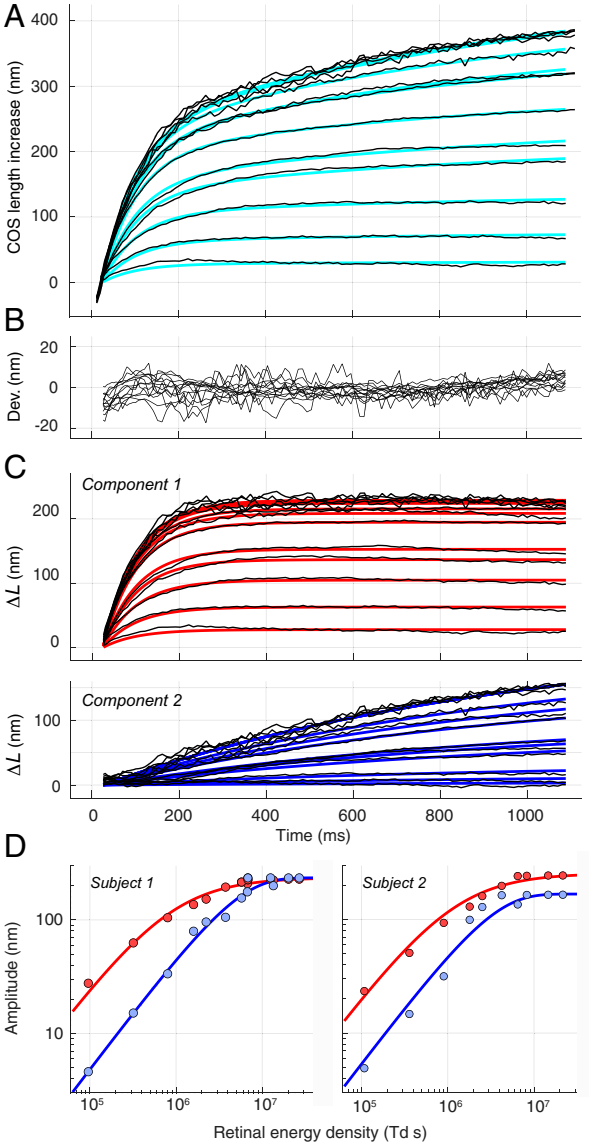

Fig. 2. COS elongation responses can be decomposed into sums of the same two exponentially rising components over the full-intensity range of the responses. (*A*) Response family from Fig. 1*B* converted to COS physical length change $\Delta L(t) = \Delta OPL(t)/n_{COS}$ with n_{COS} = 1.41, the refractive index of the COS, and fitted with weighted sums of the two exponentially rising components extracted from the fitting of the saturated COS elongation response (Fig. 1*C*). (*B*) Deviations of the traces in *A* from the fitted curves; the average RMS deviation is 4.1 nm. For a similar family of responses for subject 2 analyzed in the same manner, the average RMS deviation was 4.6 nm. (*C*) Reconstruction of components 1 and 2. In *C*, *Upper*, theoretical component 2 was subtracted from each data trace, and the residual data trace (black) was plotted along with theoretical component 1 (red traces) extracted in the fitting procedure used to generate *A*. In *C*, *Lower*, theoretical component 1 was subtracted from the data traces, and the residuals (black traces) were plotted along with component 2 theory traces (blue). (*D*) Dependence of the amplitudes of component 1 (red circles) and component 2 (blue circles) on the retinal energy density for two subjects. For subject 1, the analysis used to extract the amplitudes from the traces is illustrated in *A*–*C*; a similar response family was measured and analyzed for subject 2. The extracted amplitudes of component 1 (red symbols) are fitted with a hyperbolic saturation function, $R/R_{Comp1,\,max} = Q/(Q + Q_{50})$, and those of component 2 are fitted with an exponential saturation function, $R/R_{Comp2,\,max} = 1 - \exp(-Q/Q_e)$; the parameter values of the saturation functions of the two subjects' data are $R_{Comp1,\,max}$ = 229 nm, Q_{50} = 8.9×10^5 Td s, $R_{Comp2,\,max}$ = 235 nm, and Q_e = 4.8×10^5 Td s for subject 1 and $R_{Comp1,\,max}$ = 248 nm, Q_{50} = 1.2×10^6 Td s, $R_{Comp2,\,max}$ = 170 nm, and Q_e = 3.1×10^6 Td s for subject 2. In the small signal regime, the amplitudes of both components scale linearly with retinal energy density, and so, they can be characterized by their "rate gain," $\gamma_i = \frac{\Delta V_0}{\Delta I} = \frac{R_{i,\,max}}{\tau_i Q_i}$, where $V_0 = \frac{dR}{dt}|_{t\to 0}$ is the initial velocity of the response, ΔI is the energy density (Troland seconds), $R_{i,\,max}$ is the saturated amplitude of the component (i = 1, 2), τ_i the time constant of the exponential rise, and $1/Q_i = 1/Q_{50}$ or $1/Q_e$ is the photosensitivity of the component. The ratio γ_1/γ_2 of the rate gains is 63 for subject 1 and 54 for subject 2.

waveguide angular aperture function manifest in the Stiles–Crawford (SCI) effect, and $f_{CIS2COS} \geq 1$ expresses the energy density condensation between the CIS and the COS. The factors f_{SCI} and $f_{CIS2COS}$ vary with retinal eccentricity, but these dependencies can be estimated from previous investigations of the SCI effect (27) and histological measurements of CIS diameters (28) (*SI Appendix*, Figs. S3–S5). Three specific predictions follow from the successful application of Eq. **1**. First, the photosensitivity of the serial scanning cone reflectometry data quantified in terms of light "at the COS waveguide entrance" should be independent of retinal location. Second, the computed photosensitivity of bleaching at the COS basal disks derived by applying Eq. **1** must equal the absolute molecular photosensitivity $\alpha_{max}\gamma = 0.73 \times 10^{-8}$ μm^2 of cone opsin in situ (*SI Appendix*, Eq. **S2.7**). Third, the hypothesis that component 2 is stoichiometrically related to bleaching predicts it to have the same photosensitivity as bleaching. These predictions are borne out (*SI Appendix*, Fig. S2 and Table S1) and yield the critical conclusion that the amplitude of component 2 is linearly proportional to the quantity of bleached cone opsin.

Hypothesis: COS elongation component 2 is caused by light-induced, sponge-like swelling of cone opsin and all-trans chromophore-related disk membrane thickness increase. As possible explanations for the linear relation between bleaching and the amplitude of component 2 we considered three hypotheses: 1) a volumetric increase of cone opsin triggered by chromophore isomerization (17); 2) an expansion of the disk membranes caused by hydrolysis of the all-trans chromophore, reduction by retinol dehydrogenase (RDH), and localization of at-ROL at the cytoplasmic surface of the disk membrane; and 3) release of at-ROL into the cytosol, where it would act as an osmolyte to induce osmotic swelling (16). The third hypothesis is untenable due to the low solubility of retinol (3.5 μM; PubChem) and the latter's partitioning into the membrane (*Discussion*). The first and second hypotheses, which are not mutually exclusive, were evaluated with respect to two features of component 2: volume increase per bleached cone opsin and kinetics.

Hypothesis 1: Opsin volume expansion. Rhodopsin, the only vertebrate opsin to be crystallized to date, has a van der Waals volume of ∼47,000 Å^3 (based on structure 1U19 and the analysis in ref. 29). Given a measured COS length of 22 μm at 7° eccentricity, diameter of 1.75 μm, disk repeat period of 38 μm^{-1} (30), and opsin membrane density of 30,000 μm^{-2} (31) and assuming the human cone M-/L-opsin rest volume to be about that of rhodopsin, the total volume of the 1.2×10^8 cone opsins is 5.6 μm^3, 11% of the COS envelope volume (53 μm^3). The saturated COS elongation attributable to component 2 is 0.2 μm (Fig. 2) (average of $R_{Comp2,\,max}$ for the subjects), corresponding to a COS volume increase of 0.48 μm^3. Thus, a bleaching-induced volume increase of ∼8.5% per cone opsin is required if cone opsin swelling alone underlies the absolute magnitude and bleaching stoichiometry of component 2. Supporting this possibility, a volume change of 5% (2,200 Å^3) per opsin molecule—corresponding to the entry of 75 to 80 water molecules—has been observed upon photoactivation of rhodopsin (17). Additional support comes from circular dichroism measurements of chicken rhodopsin and chicken green cone opsin, which reveal that the cone opsin undergoes a substantially larger entropic

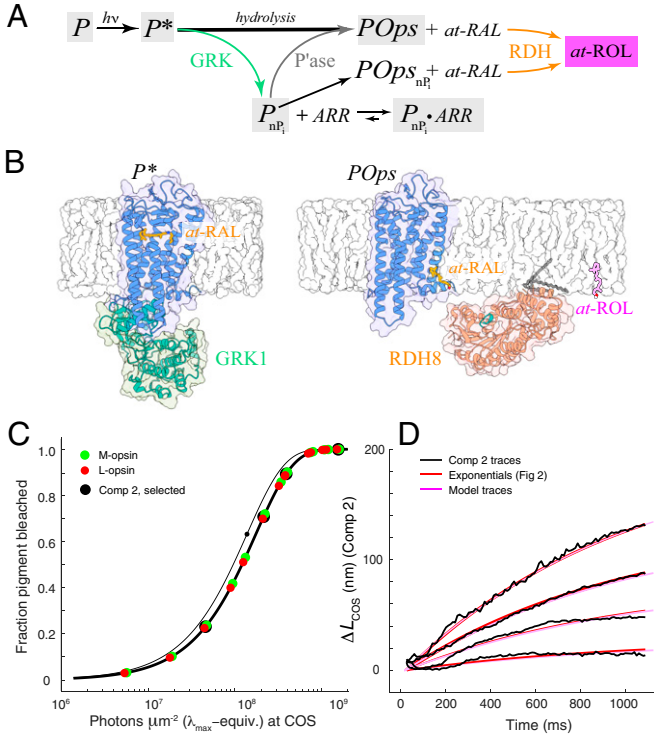

Fig. 3. Opsin and disk membrane swelling caused by chromophore isomerization, hydrolysis, and conversion to at-ROL may account for component 2 of the COS elongation response. (*A*) State space and flow schematic of reactions governing deactivation of photoisomerized cone pigment (photoactivated cone pigment [P*] = Meta II cone opsin) and production of at-ROL. At the high bleach levels that give rise to component 2, phosphorylation of P* by GRKs (including [G-protein receptor kinase] GRK1 and GRK7) is predictably saturated, and binding to P_{nPi} of arrestin (ARR) (including ARR1 and ARR7) is limited by the relatively small amount of ARR in the dark-adapted COS, so that hydrolysis of all-trans retinal chromophore becomes the dominant pathway of P* deactivation (58). RDH (RDH8 and possibly, other RDHs) is hypothesized to form a transient complex with P* to which hydrolyzed at-RAL may be weakly bound (86) and catalyzes the reduction of at-RAL to at-ROL with cofactor NADPH. (The phosphatase [P'ase] reaction, included for completeness, is unlikely to be material on the timescale of the experiments [i.e., a few seconds].) (*B*) Molecular structures of two key states in the scheme of *A*. (*B*, *Left*) GK1 bound to P* (83). (*B*, *Right*) Lipid-anchored RDH8 associates transiently with unliganded cone opsin (Pops), to whose intramembrane surface at-RAL is thought to weakly associate (86); at-RAL must diffuse to the membrane–cytosol interface and position its aldehyde group for RDH-catalyzed reduction to at-ROL. at-ROL is oriented with its dipole axis parallel to the membrane lipids (87) and should preferentially remain with its alcohol group near the membrane surface (18). (*C*) Predicted average bleaching of M and L opsin in situ in the whole COS by the stimuli used in the OCT experiments of Figs. 1 and 2 expressed in the units of energy density at the COS waveguide entrance (green and red symbols indicate M and L pigments, respectively, which are slightly differentially bleached due to their different absorption spectra). The thicker black line plots *SI Appendix*, Eq. **S2.6**, the fraction bleached over the whole COS given as the exponential approximation to the solution of *SI Appendix*, Eq. **S2.4**′, while the thin black line plots bleaching at the COS waveguide entrance (*SI Appendix*, **Eq. 2.5**), where $1/\alpha_{max}\gamma = 1.38 \times 10^8$ photons µm^{-2} is the photosensitivity of cone opsin in situ at the pigment λ_{max} and f_{Dens} = 0.79 (*SI Appendix*, Table S1). (The black symbols plot the average of the M- and L-opsin values used in the model.) (*D*) Kinetic predictions of the model. The black traces replot a subset of the extracted component 2 traces along with the fitted exponential curves (red) of Fig. 2 and the model traces (magenta). The black filled circles in *C* show the bleach levels for the specific stimuli corresponding to the traces. The topmost data trace is the saturated component 2 response; its asymptotic level is 200 nm, but this is not reached on this time base (cf *SI Appendix*, section 1).

change than rhodopsin upon photoactivation at the same temperature (32).

Hypothesis 2: Disk membrane expansion. Short-chain alcohols introduced into membranes at 1 to 2 mol % strongly increase the lateral pressure profile of phospholipid membranes near the membrane–water interface (18), a pressure increase that can cause membrane expansion. Given a phospholipid/opsin ratio of ∼65:1 (33, 34), the quantity of at-ROL generated by a full bleach corresponds to 1.5 mol % of the disk membrane lipids, in the range known to alter effective membrane thickness (18). A 22-µm-length COS at 7° eccentricity comprises 1,660 disk membrane bilayers, so if the bilayer thickness increase caused by at-ROL is the sole mechanism underlying of component 2, the saturated COS length increase of 200 nm requires a thickness change of 0.12 nm per bilayer, 2.4% of the ∼5-nm bilayer thickness. Moreover, because the van der Waals volume of all-trans retinal is ∼300 Å^3, its hydrolysis and displacement into the lipid bilayer per se may produce an ∼600-Å^3 net volume increase in the membrane, even before all-trans retinal (at-RAL) reduction to at-ROL.

Component 2 rises exponentially with a time constant of ∼1 s (Figs. 1 and 2), and so, the underlying molecular process should exhibit this time constant. Rhodopsin swelling is associated with the spectroscopically identified metarhodopsin II state (17), whose time constant of appearance is ∼1 ms in both rods and cones (35–37). While this latter observation weighs against hypothesis 1 in its simplest form, hydration consequent to meta II state of cone opsin (Meta II) formation may be much slower than the spectral transition, and the hydration and swelling attendant chromophore hydrolysis and at-RAL exit from the binding pocket—which takes minutes in rods but seconds in cones (35, 36, 38, 39)—may be similarly slow. Importantly, hypotheses 1 and 2 are not mutually exclusive. Accordingly, we propose that the mechanism underlying component 2 is cone opsin and disk membrane swelling arising from hydrolysis of the all-trans chromophore, the latter's reduction by RDH at the cytoplasmic surface, and attendant water-induced membrane swelling, with these combined processes rate limited by chromophore hydrolysis having a time constant (∼1 s) matching that of component 2 (Fig. 3).

Hypothesis: COS elongation component 1 corresponds to phosphate (P_i) produced by RGS9-1–catalyzed hydrolysis of GTP in $G_{tc}\alpha$–PDE complexes and removal by glyceraldehyde-3-phosphate dehydrogenase. The light dependence and gain of component 1 (Fig. 2) imply that the mechanism underlying this component of COS elongation involves an amplified by-product of phototransduction. Several molecular hypotheses can be tested within the framework of the osmoelastic hypothesis (16), which postulates that the outer segment swells in response to an increase in cytoplasmic osmolarity and which provides a gauge of a 0.027-mOsM/nm increase in COS length (*SI Appendix*, section 3). Straightforward considerations reject the soluble by-products of several candidate reactions, including G-protein moieties dissociating into the cytosol from the disk membranes, metabolites of cGMP hydrolysis, metabolites of low Ca^{2+}-stimulated guanylate cyclase synthesis of GTP, ionic concentration changes arising from the closure of the COS cyclic nucleotide (CNG)-gated channels, and subsequent ionic changes accompanying membrane hyperpolarization (*SI Appendix*, section 6). One amplified phototransduction by-product that is not readily rejected and calls for more detailed evaluation as a candidate for component 1 is P_i generated by RGS9-1–catalyzed hydrolysis of GTP in the complex of activated phosphodiesterase with the activated α-subunit of the G protein ($G_{tc}\alpha$–GTP–PDE) (40, 41) (Fig. 4 *A* and *B*). This hypothesis is suggested by several distinctive aspects of the RGS9-catalyzed GTPase reaction in cones. First, cones are known to express RGS9-1 at much higher levels than rods (42, 43), and the experimentally manipulated RGS9 expression level dictates the maximum velocity V_{max} of the GTP hydrolysis reaction in living rods (44, 45).

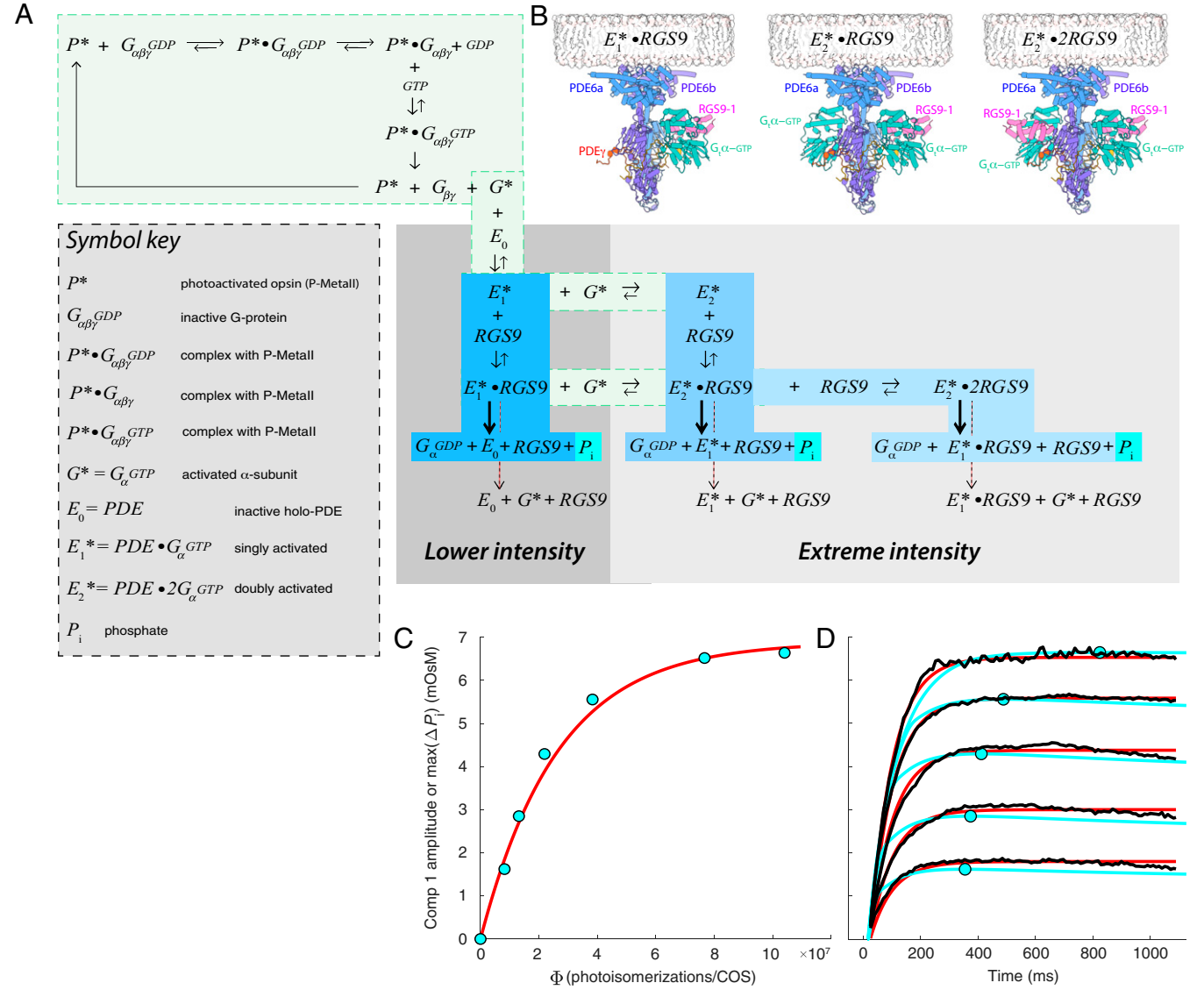

Fig. 4. Reactions governing the production of P_i by RGS9-catalyzed GTP hydrolysis and P_i recycling by GAPDH in the glycolytic cycle can explain the light sensitivity, kinetics, and magnitude of component 1 of the COS elongation response. (*A*) State space and flow schematic of phototransduction reactions leading to the production of P_i. The pale green rectangle in the upper left portion of the schematic highlights the cycle by which the isomerized G protein coupled receptor (GPCR) P* catalytically activates its G protein, producing G* ($G_t\alpha$–GTP). The blue-box regions highlight reactions involving G* and phosphodiesterase (PDE dimer) in six distinct states, depending on binding partners: E_0, unliganded/inactive; E_1*, partially activated by binding of one G*; E_2*, fully activated by binding of two G*; E_1*•RGS9, E_1* with one RGS9 complex bound; E_2*•RGS9, E_2* with one RGS9 complex attached; E_2*•2RGS9, E_2* with two RGS9s bound. For lower-intensity stimulation, the reactions in the dark gray rectangle predominate; as intensity increases to the extreme levels of the optoretinography (ORG) experiments, the increased production of G* drives the reactions to the right (the lighter gray region of the diagram). (*B*) Molecular structures of the three complexes that generate P_i (cyan highlights) by RGS9-catalyzed GTP hydrolysis of $G_{tc}\alpha$–GTP bound to a PDE6 catalytic subunit: E_1*•RGS9, E_2*•RGS9, and E_2*•2RGS9. (In *A*, the dashed arrows show the possible paths arising from G* dissociation from the three complexes without GTP hydrolysis, and the colored rectangles serve to visually isolate portions of the reaction scheme.) (*C* and *D*) Predictions of the reaction scheme. The scheme was embodied in a system of ordinary differential equations and solved for different flash strengths (*SI Appendix*, section 4). In *C*, the predicted maximum level of ΔP_i for a subset of intensities (cyan-filled circles) is compared with an empirical hyperbolic saturation function (red curve) that describes the amplitude of component 1 when plotted as a function of the number of photoisomerizations (Φ) per COS. $\Phi = 1.2 \times 10^7$ photoisomerizations corresponds to an equimolar quantity of P* and total G protein (i.e., one P* for every G protein in the COS). In *D*, the component 1 responses (black traces) to this subset of intensities are plotted along with the exponentials originally fitted to them (red traces) (Fig. 2*C*) and the increases in P_i, $\Delta P_i(t)$ (cyan traces), predicted by the model (the measured traces for the two most intense flashes were effectively indistinguishable and were averaged). Symbols in *D* plot the maximal amplitudes of the model traces (cyan). Note that *C* and *D* share the same ordinate scale and units.

Second, the lifetime τ_E of the catalytic complex $G_{tc}\alpha$–GTP–PDE in humans and nonhuman primate cones has been estimated with models of the cone electrical response to be 8 to 15 ms (43, 46, 47). As τ_E corresponds to the reciprocal of the single-enzyme turnover of the RGS9 reaction (44), in cones RGS9 appears capable of catalyzing P_i production at a rate of 100 s^{-1} or more. Third, glyceraldehyde-3-phosphate dehydrogenase (GAPDH), a key enzyme of the glycolytic cycle that regenerates NADPH and recovers P_i for triphosphate synthesis, is present at high levels and is functional in outer segments (48, 49). To see how exponentially rising kinetics could arise from P_i production by RGS9-catalyzed GTP hydrolysis and removal by GAPDH, consider the following rate equation:

$$\frac{d\Delta P_i(t)}{dt} = [RGS9]\, k_{cat} - k_{P_i}\, \Delta P_i(t). \qquad [2]$$

In Eq. **2**, $\Delta P_i(t) = P_i(t) - P_{i,\,rest}$, with $P_{i,\,rest}$ the resting level of P_i; $[RGS9]$ the enzyme concentration referred to the

cytoplasmic volume; k_{cat} the RGS9 turnover number; and $k_{P_i} = V_{max,\,GAPDH}/K_{m,\,GAPDH}$ the effective rate constant of the final step in the GAPDH catalytic cycle, for which P_i is a substrate (ref. 50, pp. 298–299). For stimuli that produce a saturating component 1 response, the number of isomerized cone opsins (P*) in the COS exceeds the total quantity of G protein, which in turn, exceeds the total quantity of PDE. As a consequence, in the phototransduction response to such intense stimuli, all PDE catalytic subunits will rapidly bind a activated G-protein alpha subunit (G*) and thereby become substrates for the RGS9 GTPase reaction within a few milliseconds; moreover, the P* will predictably produce G* in excess of the number of PDE catalytic subunits, leading to a persistent, maximum GTPase velocity, $[RGS9]\,k_{cat}$. Under such conditions, the solution to Eq. **2** is a rising exponential function,

$$\Delta P_i(t) = \Delta P_{i,\,max}[1 - \exp(-k_{P_i} t)], \qquad [3]$$

consistent with the results (Fig. 2*C*), with $\Delta P_{i,\,max} = [RGS9]_{tot}\,k_{cat}/k_{P_i}$. The saturating level of component 1 responses yields the estimate $\Delta P_{i,\,max}$ = 6.5 mM, and given k_{P_i} = 12.8 s^{-1} ($k_{P_i} = 1/\tau_1$) (Fig. 1*C*), the maximum velocity of GTP hydrolysis is $V_{max,\,RGS9} = [RGS9]_{tot}\,k_{cat}$ = 83 mM s^{-1} for subject 1 and 73 mM s^{-1} for subject 2. The analysis embodied in Eqs. **2** and **3** thus explains the saturation of component 1 with light intensity as arising from complete and continued activation of PDE by G* combined with saturated binding of RGS9 to the activated PDE catalytic subunits, which drives RGS9-catalyzed GTP hydrolysis to its maximum velocity.

We next sought to determine whether the RGS9–GAPDH hypothesis could be extended to explain the graded behavior of component 1 over its full-intensity response range (Fig. 2 *C* and *D*). The graded amplitudes imply that different bleaching levels in the intensity range of production of component 1 generate different steady levels of P_i between ∼200 and 1,000 ms. To investigate how this behavior might arise, we developed a model of phototransduction with features that embody the extraordinary ability of cones to function in light levels that bleach large fractions of their pigment (Fig. 4 *A* and *B*; cf *SI Appendix*, Figs. S6 and S7). The model comprises several interconnected "reaction units" (Fig. 4*A*, colored boxes). The uppermost unit of reactions (Fig. 4*A*, pale green rectangle) schematizes the G-protein activation cycle driven by P*, the photoactivated GPCR. The output of this cycle, activated G protein (G* = G_{tc}α–GTP), drives activation of PDE by formation of activated PDE catalytic subunit (E*) (G*–PDE) complexes (Fig. 4*A*, blue boxes); these complexes, in turn, are the substrate for RGS9-catalyzed GTP hydrolysis and P_i production (Fig. 4*A*, highlighted in cyan). The activation of single catalytic subunits of the PDE holodimer (Fig. 4*B*; darker gray rectangle in Fig. 4*A*) governs the reactions for lower-intensity stimuli; thus, for example, a stimulus producing 10^6 P* per COS (∼0.8% bleach) is predicted to activate single PDE catalytic subunits at a ratio of 36:1 relative to doubly activated subunits. At the extreme intensities that produce component 1, however, the increasing amount of G* activates both PDE catalytic subunits (Fig. 4), increasing the substrate for RGS9-catalyzed GTP hydrolysis. The model generates a reasonable account of the light dependence and kinetics of both component 1(Fig. 4 *C* and *D*) and component 2 (Fig. 3 *C* and *D*). Key features of the model for generating approximately steady P_i levels with appropriate light dependence (Fig. 4 *C* and *D*) are rate-limited (saturated) phosphorylation of P* by G-protein receptor kinase (GRK) and an ∼10-fold reduced ability of phosphorylated opsin (P_{nPi}) and unliganded opsin (POps) to activate G protein (*SI Appendix*, Fig. S7). Notably, with the same parameters, the model can provide a good account of the human cone electrical response (*SI Appendix*, Fig. S8 and section 5). The prediction of the electrical response constrains multiple parameters of the model and provides evidence that RGS9 catalysis of singly activated PDE catalytic subunits (Fig. 4 *A*, the "lower-intensity" portion of the schematic and B, E_1*●RGS9) governs deactivation of the cone electrical response for low bleach levels.

Discussion

Human COSs elongate in response to strongly bleaching light stimulation (Fig. 1*B*) (8, 9). The elongation responses to stimuli ranging ∼200-fold in intensity up to the level that completely bleaches the cone pigment are well characterized as the sum of two exponentially rising components over their entire dynamic range (Fig. 2). Comparable in saturated amplitudes, component 1 has a maximal velocity 13-fold greater than component 2, is 3- to 6-fold more sensitive to light, and has a more than 50-fold higher small signal rate gain (Fig. 2*D*). Identification of the biochemical reactions and molecular species underlying the two kinetic components clearly enhances the value of COS elongation measurements both for understanding human cone photoreceptor function in vivo and for clinical applications of optoretinography (ORG) in quantifying the progression of cone-blinding eye diseases, such as age-related macular degeneration, and in assessment of therapeutic interventions in such disease.

Cumulative advances in the biochemistry and physiology of rod and cone phototransduction and their retinoid cycles provide a basis for formulating and testing hypotheses about the molecular identities underlying the COS elongation response components. A critical problem that must be addressed in any effort to predict the molecular events of COS elongation responses is that the quantities and kinetics of phototransduction by-products necessarily depend on the precise amount of P* (photoisomerized/bleached pigment) produced by each stimulus, particularly in the high-bleaching regime in which various key enzymes and substrates in the phototransduction cascade are predictably saturated or depleted. In particular, for cones at the retinal locus of the present OCT experiments, precise calculation of P* from stimuli measured at the pupil is problematic due to several factors known to vary with retinal eccentricity. To address this problem, we measured bleaching at the retinal locus of the OCT measurements (*SI Appendix*, Fig. S2).

Cone Pigment Photosensitivity Can Be Accurately Measured with AO-SLO Serial Scanning Single-Cone Reflectometry. The discrepancy between the photosensitivity of component 2 and previous foveocentric measurements of the cone pigment bleaching photosensitivity measured in retinal illuminance units (*SI Appendix*, Fig. S2*D*) led us to undertake bleaching measurements with AO-SLO serial scanning single-cone reflectometry in the same eyes and retinal location (7° temporal) as the OCT ORG (*SI Appendix*, Fig. S2 *A–D*) and in other locations closer to the fovea. We hypothesized that the apparent discrepancies arose in large part from the use of the Troland unit of retinal illumination, which implicitly assumes that light entering the eye from all positions in the pupil is equally available to isomerize cone pigment—an untenable assumption given the broadly accepted thesis that the SCI effect is a direct manifestation of the steep angular aperture function of the cone waveguide (51–54). Thus, the problem posed by discrepant photosensitivities (*SI Appendix*, Fig. S2*D*) was recast as a question of whether

reasonable eccentricity-dependent factors (Eq. **1** and *SI Appendix*, Eq. **S2.7**) could be found that could convert all measured photosensitivities attributable to bleaching to one and the same intrinsic photosensitivity at the COS waveguide entrance (i.e., at the basal cone disk membranes). The analysis showed this to be possible (*SI Appendix*, Fig. S2*E* and Table S1), a result validating AO-SLO serial scanning single-cone reflectometry as a method for measuring the photosensitivity of cone pigment bleaching at different eccentricities and establishing the equivalence of the photosensitivity of component 2 with that of cone pigment bleaching.

Identification of Component 1 as P_i Produced by RGS9-1–Catalyzed GTPase and Removed by GAPDH. Three striking and defining features of component 1 are its rapid exponential rise (τ = 80 to 90 ms), its subsequent ∼10-fold longer plateau (Fig. 2*C*), and the grading of its amplitude with bleach level (Fig. 2*D*). The features of the component 1 saturated response can be explained in terms of production of P_i by maximal RGS9-catalyzed GTPase activity and removal by GAPDH (Eqs. **2** and **3** and Fig. 4 *C* and *D*). The deduced maximal RGS9 catalytic activity, ∼80 mM s^{-1}, is extraordinary but broadly consistent with expectations based on the much higher level of RGS9 expression in cones than in rods (42, 43), from results and analysis showing that the GTPase reaction rate scales with RGS9 expression (44, 45), and from the ∼10-ms "single-turnover" time (τ_E) of the reaction in human and primate cones estimated with models of the electrical response (46, 47, 55) (*SI Appendix*, Fig. S8 and section 5). Parsimony suggests that the same molecular mechanism should underlie component 1 over its full dynamic range (Fig. 2*D*), a challenge for phototransduction theory, which has not previously been applied to cone function in response to such extreme bleaching exposures. Incorporating only known outer segment proteins and complexes and reaction rates informed by the extreme intensities, the model provided a reasonable account of component 1 (Fig. 4*D*) and of the human cone electrical response at far lower intensities (*SI Appendix*, Fig. S8). Attributing component 1 to an osmotic response also provides an estimate of COS membrane water permeability: 0.0014 cm s^{-1} (*SI Appendix*, section 3). The COS plasma membrane water permeability is thus at least 50-fold greater than that of the rod (16), a comparative result discussed further below (cf *SI Appendix*, section 7).

Mode Switching and Reactant Recycling Contribute to the Extraordinary Capacity of Human Cones to Function in Extreme Light. Human cones possess the extraordinary capabilities of signaling in steady light that bleaches a large fraction of their pigment and of recovering very rapidly the ability to signal after an extreme bleaching exposure (21, 56, 57). COS elongation responses measured with OCT ORG (Figs. 1–4) enable these capabilities to be investigated in individual cones in vivo and can provide insight into the underlying molecular processes. A broad insight from the modeling effort is that in response to bleaching stimuli in the intensity range that triggers COS elongation, key enzymatic reactions switch from a low-substrate concentration mode to a saturating-substrate mode. This "mode switch" facilitates overall recovery from intense stimulation and recycling of molecular by-products critical for phototransduction as follows.

For the intense stimuli that give rise to component 2 (Fig. 3*C*), the model predicts that deactivation of P* switches from the GRK/arrestin (ARR) pathway that dominates at lower intensities to hydrolysis of the all-trans chromophore (Fig. 3*D*) (58). This switch is necessitated by the limited quantities of GRK and ARR in the dark-adapted outer segment (*SI Appendix*, Table S2) and ensures more rapid recycling of both opsin and chromophore. Thus, were GRK phosphorylation of P* and ARR binding able to completely deactivate all the P* from a full bleach as quickly (<10 ms) as these reactions do at low to modest intensities, dissociation of ARR from cone phospho-opsin (P_{nPi}) even 100-fold faster than that measured for ARR1 dissociation from phosphorhodopsin (59) would leave us blind for minutes.

For the stimuli that give rise to component 1 (Fig. 4*C*), the model predicts that persistent activation of G protein by the combined activity of P*, all-trans retinal-liganded cone phospho-opsin (P_{nPi}), and POps switches the GTPase reaction from singly activated RGS9 complexes (Fig. 4 *A*, "lower intensity" and *B*, "E_1*•RGS9") to doubly activated, doubly RGS9–bound complexes (Fig. 4 *A*, "extreme intensity" and *B*, "E_2*•2RGS9"; cf *SI Appendix*, Fig. S6). Driven by persistent G-protein activation and rapid deactivation via RGS9 (44), during the ∼1-s epoch of component 1, GTP hydrolysis achieves a steady rate determined by the level of G*, as manifested by the steady levels of P_i (Fig. 4*D*; cf *SI Appendix*, Fig. S7). The P_i produced is then presumably rapidly recycled via GAPDH and the rest of the glycolytic pathway (48, 49) and by phosphotransferases in the outer segment, such as nucleoside diphosphokinase 1 and 2 (NME1 and NME2) (60), that regenerate adenosine triphosphate and GTP for use in cGMP synthesis, phosphorylation, etc.

Rod vs. Cone Elongation Responses: Opsins as Sponges and Water Conduits. Both rods and cones generate ORG responses that include outer segment elongation and scattering changes in response to stimuli that bleach substantial fractions of their respective opsins (8, 9, 16, 61). The elongation responses of the two types of photoreceptors differ substantially in saturated magnitude, light (bleaching) sensitivity, and kinetics, with the elongation responses of rods being larger, more sensitive to light, and much slower to develop than those of cones. Nonetheless for these quantitative differences, rod and cone elongation responses appear to share several common mechanisms (*SI Appendix*, Table S1). Here, we consider one of the most fundamental common mechanisms: water movement into ("sponge") and through ("conduit") photo-activated opsins. (A more extensive comparison is provided in *SI Appendix*, section 7.) Accordingly, vertebrate opsin function comprises two parallel and interacting cycles that enable them to repeatedly capture light and signal, the chromophore cycle and the water cycle, and different quantitative features of these linked cycles underlie the distinctive elongation responses of rods and cones.

Dark-Adapted Dehydration of the Inverse-Liganded Opsin. In the dark-adapted state, water access to the Schiff base lysine bond of the chromophore on transmembrane (TM) helix VII must be severely restricted to prevent spontaneous hydrolysis. Restriction of water access to the chromophore bond requires dehydration of the inverse-liganded structure but more stringently so in rhodopsin than in cone opsins because ligand-free rod opsin activates G protein to a degree that could overwhelm single-photon signaling (35, 62, 63). Dehydrated opsin can be thought of as a dry sponge, ready to take up water (17) and to transport it across the membrane (64) when the tap is flipped open by photoisomerization-induced conformational changes (17) and there is a transmembrane osmotic gradient (16).

Photoisomerization-Induced Increase in Water Influx and Hydrolysis of the All-Trans Chromophore. Photoisomerization triggers large structural changes in rhodopsin, including substantial displacements of TM5 and TM6 relative to adjacent helices

(65). Water diffusing into the photoactivated opsin accompanies and sustains these structural changes (17, 65) and hydrolyzes the chromophore bond, a reaction that takes minutes in rods (35) but seconds or less in cones (36, 39, 66). The "hydrated sponge" form of the opsin also creates a transmembrane water conduit (64) that can enable osmotic equilibration across the membrane. Water movement through metarhodopsin across the internalized rod disk membrane may explain the relatively large increase in osmotic pressure inferred to occur in mouse rods (16). Thus, during its biosynthesis (67), the internal space of the rod disk may trap extracellular solutes that become osmotically inactive as disks seal and dehydrate under structural tension but become osmotically active with respect to the cytoplasm when metarhodopsins form transmembrane water conduits. The much faster hydrolysis of the all-trans chromophore in cones suggests that maximum water permeability of photoactivated cone opsin is achieved more rapidly than in rhodopsin (cf *SI Appendix*, section 3). A puzzling feature of the mouse rod ORG that may find explanation in the water sponge–conduit hypothesis is the dependence of the rod elongation response on the G protein (16). Chawla et al. (17) report that a peptide mimicking the portion of the G protein that binds to metarhodopsin II during activation causes substantially increased swelling, and thus, it is plausible that metarhodopsin is a more permeable transmembrane conduit in the G protein–bound state and that this more permeable state may persist after the G protein dissociates.

Pigment Regeneration by 11-Cis Retinal and Opsin Dehydration. The opsin chromophore cycle is completed when the hydrolyzed all-trans chromophore exits the binding pocket and 11-cis retinal enters and reestablishes its covalent bond to the target lysine. The waters that hydrated the opsin sponge must be squeezed out, and the transopsin water channel(s) must be blocked to allow the Schiff–base bond to reform and be protected from hydrolysis. Given that ∼50% of the disk membrane area is occupied by opsins (31), it is plausible that the water content of the COS disk membrane bilayer with its dense opsin concentration cycles in a manner that alters its thickness (68) to the estimated extent of 0.12 nm per disk face (Fig. 4).

Unresolved Questions and Examples of Further Tests of the Hypotheses. Numerous unresolved questions about rod and cone ORG responses remain to be formulated in terms of mechanistic hypotheses at the atomic, cellular, and tissue levels, and experiments need to be designed to test them. For example, the hypothesis that component 1 arises from P_i produced by RGS9-catalyzed GTP hydrolysis might be tested in patients with bradyopsia arising from defects in RGS9 (69–71), and if successful, it would support the use of component 1 to assess several critical COS enzymatic activities and their substrates. The hypothesis that component 2 arises from water entering photoactivated cone opsins whose hydrolyzed chromophore has exited the binding pocket may be testable with parallel OCT and two-photon retinol fluorescence imaging (72, 73). In closing, it is remarkable that the ORG (Figs. 1 and 2) and serial scanning reflectometry (*SI Appendix*, Fig. S2) may not only manifest aspects of the phototransduction cascade (Fig. 4) and the retinoid and water cycles of the opsins but also, allow them to be investigated in vivo in single cones and rods in normal and diseased states.

Materials and Methods

Subjects. Two male subjects (ages 37 and 44) free of retinal disease participated in the study after cycloplegia with tropicamide 1% ophthalmic solution (Akorn Inc.). The research was approved by the University of Washington institutional review board, and subjects signed an informed consent before their participation and after the nature and possible consequences of the study were explained. All procedures involving human subjects were in accordance with the tenets of the Declaration of Helsinki.

OCT Measurement of Light-Induced COS Length Changes. An AO OCT system described elsewhere (74) was used for measuring light-induced COS changes. In brief, a superluminescent diode (λ_o = 840 nm, $\Delta\lambda$ = 50 nm, 6.2-μm axial resolution in air, MS840BI20; Superlum) was used as illumination for OCT and for line-scan ophthalmoscopy (LSO), a 980- ± 10-nm (IPSDD0906; Inphenix) source was used for wave-front sensing, and a 528- ± 20-nm light emitting diode (LED) in Maxwellian view was used for retinal stimulation. A line field on the retina was generated using a cylindrical lens (ACY254 100B; Thorlabs Inc.) and scanned with a 1-dimensional galvo scanner (6210H; Cambridge Technology) to acquire volumetric OCT. A custom-built Shack–Hartmann wave-front sensor and a deformable mirror (Alpao; DM9715) were incorporated into the optical path to correct the eyes' optical aberration. The eye's pupil, the scanner, and the deformable mirror were optically conjugated using achromatic lens-based afocal telescopes. In detection, a 1,200–line pairs/mm diffraction grating, an achromatic lens, and a high-speed 2-dimensional camera (pixel size, 20 μm; FASTCAM Mini Ax200; Photron) formed the OCT spectrometer. The zeroth order beam of the grating, which is usually discarded in a traditional spectral domain OCT, was used to construct an LSO by placing a focusing lens and a line-scan camera. Because the LSO sensor was optically conjugated to the OCT imaging camera, the en face LSO images were also used to optimize the focus on cone photoreceptors for imaging. The power was 3.2 mW at the cornea. Custom LabVIEW software was used to synchronize the scanner, frame grabbers, and data acquisition, enabling live image visualization and real-time feedback to the experimenter for subject alignment. For measuring COS changes, an artificial iris reduced the imaging beam diameter to 4 mm, real-time AO correction of higher-order aberration was turned off, and either the deformable mirror or trial lenses were used to optimize focus for cone photoreceptors. A 0.6° × 1.4° field of view centered at 7° temporal eccentricity was imaged. Subjects were dark adapted for 4 min prior to acquiring OCT volumes for 1 to 2 s at 120 volumes/s. After a delay of 10 volumes, the 528-nm LED illuminated the retina in Maxwellian view for durations ranging from 3 to 70 ms; combined with calibrated neutral density filters, this provided controlled intensity. Each OCT trace presented in the MS represents the average of three to four individual runs for the same bleaching exposure. At least 5 min of dark adaptation was required between each bleaching exposure, considerably lengthening the time that needed to be committed to complete a full-intensity series covering a 200-fold range. The OCT experiments of each subject required at least two extensive sessions on successive days and required highly skilled observers who could maintain fixation over lengthy sessions. The same subjects also participated in even more extensive and time-consuming bleaching experiments (below). For these reasons and because the data obtained were highly reliable and overall consistent between observers, we limited the OCT experiments to two subjects.

OCT image processing followed conventional techniques. Acquired OCT data were resampled in k-space and Fourier transformed along the wave-number dimension to extract complex-valued retinal volumes. Each OCT volume was segmented, and en face images were obtained by taking the maximum-intensity projections centered at the cone outer segment tip (COST) for visualizing the cone photoreceptors. En face images were registered using a strip-based registration algorithm (75), with lateral shifts from the en face registration, and axial shifts from segmentation were used to register all volumes. For measuring COS length changes, the registered OCT volumes were referenced to the mean of all volumes recorded before the stimulus onset to cancel arbitrary phase noise and set a baseline. From these referenced volumes, a three-pixel mean of complex values centered at the backscatter bands of the inner segment - outer segment (ISOS), and COST was calculated. The phase difference between these two layers was calculated by multiplying the complex conjugate of the COST value with that of the ISOS and calculating the argument of the resulting product. For phase responses that exceed $\pm\pi$ radians, phase was unwrapped along the time dimension at each pixel. The change in OPL was calculated by the relation $\Delta OPL = (\lambda_o/4\pi) \times (\Delta COST - \Delta ISOS)$, where λ_o = 840 nm and ΔCOST, and ΔISOS are the phase changes from baseline for the COST and ISOS bands.

Average COS lengths as well as length changes were extracted from the OCT data at each of the eccentricities. Averaged over four subjects and adjusted for a COS refractive index of 1.41, the outer segment lengths were 38.3 ± 2.4, 29.5 ± 2.4, and 21.9 ± 0.6 μm (mean ± SD) for 1.5°, 4.5°, and 7° temporal eccentricities, respectively. These length measurements were used in calculating COS pigment axial densities involved in quantifying bleaching (Fig. 3 and *SI Appendix*, Fig. S2*C*).

AO-SLO Serial Scanning Single-Cone Reflectometry. An AO-SLO described elsewhere (76) was used for serial scanning reflectometry. Briefly, wavelengths bands–520 ± 25 and 900 ± 16 nm–were selected from a supercontinuum laser source (SuperK Extreme; NKT Photonics) with a combination of long-pass and narrowband interference filters. The 900-nm beam was used for AO closed-loop correction using a custom Shack–Hartmann wave-front sensor and a deformable mirror (Alpao; DM9715). The 520-nm beam was used for serial scanning reflectometry to compare against light-induced COS changes measured with 528-nm stimuli. Light scattered from the retina was similarly split into separate collection assemblies for each wavelength. The 520-nm light scattered from retina was collected in a photomultiplier tube via a confocal pinhole and rendered into a continuous video stream of the retina at 30 Hz, allowing a measure of dynamic changes in cone reflectance following dark adaptation. The beams were raster scanned using a resonant and galvo scanner to generate a 1.0° or 1.2° square imaging field centered at 1.5°, 4.5°, and 7° temporal eccentricities. The eye's pupil, the scanner, and the deformable mirror were optically conjugated using reflective mirror–based afocal telescopes. Subjects were dark adapted for 4 min prior to a 520-nm imaging. The imaging beam size at the pupil was 6 mm in diameter. Following dark adaptation, the subjects were first aligned using the 900-nm wavelength and optimized for optimal AO closed-loop performance. Once optimal AO performance was reached, as evaluated via the computed wave-front RMS and Strehl ratio, the 520-nm imaging light was switched on to image the retina for 4 s.

The processing of AO-SLO reflectance videos followed from previous work (25). Briefly, the videos were registered via a strip-based image registration algorithm. The maximum region of interest, uncorrupted by eye motion, and occluding blood vessels was selected from an averaged high signal-to-noise ratio retinal image, and cone locations were identified within this region. The mean image intensity within a 0.6–arc-min square area surrounding the cone center was tracked over time in the registered video and normalized. The image intensity vs. time was analyzed as described previously (77, 78) and in Fig. 3 to extract B_0, the nominal fraction of cone pigment bleached per scan.

Calibration of Light Stimuli. Light stimuli were measured radiometrically at the plane of the pupil with a calibrated UDT-247 photodiode with a 1-cm^2 sensor area operating in the photovoltaic mode; this sensor has a very flat spectral responsivity over the range of the stimuli. The spectra of the light stimuli were measured at the pupil plane with a spectroradiometer (CS-2000; Konica Minolta). For the OCT experiments, the light source was a CREE X-lamp-E green light-emitting diode (part XPEGRN-L1-R250-00C01; Digi-Key) with a 39-nm bandwidth (full width at half-maximum) centered on 528 nm. A custom LED driver board was used to control the intensity of the LED and to interface timing with the OCT system. The driver board pulse frequency modulation control and LEDs were mounted on aluminum heat sinks that ensured that the spectral output of the LEDs did not shift as a function of intensity. The rise time and fall time of this LED were measured with a fast photodiode (ODD-5WISOL; Opto Diode Corp.) and found to be 2.5 and 5 μs, respectively. For AO-SLO serial scanning reflectometry, a bandpass filter centered on 520 nm (FF02-520/28-25; Semrock) was used to filter the supercontinuum source. The angular size of the Maxwellian stimulus at the retinal plane was measured by placing an artificial eye with a focusing lens, with an image sensor at the image focus. The angular extent of the AO-SLO scanning raster was determined by imaging a grid target (0.125-mm spacing, 59-209; Edmund Optics) placed at the retinal plane of the artificial eye. For the AO-SLO beam, the spatial distribution of power at the pupil plane was derived from power measurements taken as the diameter of a mechanical iris at a conjugate plane varied from 1 to 7 mm. Similarly, for the LED source used in the OCT experiments, the distribution at the pupil plane was obtained from measurements made with an iris that was varied from 1 to 15 mm in diameter. The power distributions in the pupil plane were needed for calculating the power captured by the CIS waveguides (*SI Appendix*, Fig. S3).

Conversion between Photometric, Radiometric, and Photoisomerization Units. To facilitate comparison of cone pigment bleaching produced by the stimuli in our experiments with those in previously publications, we employed the conventional photometric energy density unit (Troland seconds), where 1 Td s = 10^{-6} lumens $sr^{-1}$of visual (79). The photometric fluxes (lumens) of the stimuli were derived from the spectral power densities (watts $nanometer^{-1}$) of the stimuli at the corneal plane integrated at 1-nm resolution against the CIE photopic visibility curve V(λ) (www.cvrl.org/; "linCIE2008v2e_1") and multiplied by the luminous efficiency factor K_m = 683.02 lm W^{-1}. The solid angles of the stimuli were computed from the angular areal subtense (degrees squared) of the retinal images with the conversion factor 3,282.8$^{\circ 2}$ sr^{-1}.

Calculation of the rate of photon capture by cones from the retinal energy density is problematic because relevant properties of cones–including their angular aperture function at the pupil (SCI effect) and the condensation of light energy density between the wider CIS and the narrower COS–involve waveguide properties that vary substantially with eccentricity. Consequently, conversion from Trolands to cone pigment bleach rate at different retinal eccentricities requires an approach that identifies and estimates the factors affecting the conversion. This effort is applied in the presentation of AO-SLO serial scanning single-cone reflectometry data (*SI Appendix*, Fig. S2) and is explained in *SI Appendix*. Based on measurements of the spectra of the sources, the distribution of light at the pupil plane and the distribution of light at the plane of the retina, the factors of Eq. **1**, and the size and pigment densities of the COS, the prebleach conversion factor derived from the AO-SLO serial scan bleaching is ∼70 photoisomerizations (Td s)$^{-1}$ for the 7° temporal eccentricity bleaching target.

Molecular Model of Cone Phototransduction for Predicting COS Elongation. To test hypotheses about the molecular identity of the osmolytes corresponding to components 1 and 2 of COS elongation responses, we developed a model of cone phototransduction to predict the kinetics and absolute light sensitivity of the osmotic response. The model is conventional in the sense that all reactions and reactants involved are established to be present in rod and cone photoreceptors and have (to varying degrees) been characterized with biochemical and physiological assays. The variables, rate equations, and kinetic parameters of the model are provided in *SI Appendix*, section 4. The stimuli used are estimated to isomerize/bleach fractions of M- and L-cone pigment ranging from 0.005 to 0.99. During the reactions to such stimuli, the absolute quantities of several key macromolecular components–including inactive M and L opsin, inactive heterotrimeric G protein, and inactive PDE catalytic subunits–can become exhausted, affecting rates and altering the reaction pathways in a stimulus-dependent manner. Where possible, cone-specific information from nonhuman mammalian species was used to set resting quantities and maximal rates–for example, the much higher expression level of RGS9-1 in cones than in rods (42) is critical, as is the much higher activity of RDH (66). The model with unchanged parameters was also tested against human cone photoresponses recorded with the electroretinogram (ERG) *a* wave in response to stimuli far less intense (46, 55) than those involved in the COS elongation response (*SI Appendix*, section 4).

Protein Structural Models. Structural models are used to illustrate key macromolecular complexes involved in or affecting the production of the osmolytes hypothesized to underlie COS elongation responses (Figs. 3*B* and 4*B*) and to illustrate reactions and molecular states of the dynamic model.

In Fig. 3*B*, RosettaCM (80) was used to generate homology models of human M opsin in key states: P* (fully activated Meta II state; Protein Data Bank [PDB] ID codes 3PQR and 7MTB are used as templates) and POps (ligand-free cone opsin; PDB ID code 3CAP used as a template). The top scoring models of P* and POps were aligned to the oriented templates obtained from the Orientation of Protein in Membranes (OPM) database (81) to translocate the models into membrane coordinates. The CHARMMGUI server (82) was then used to embed the oriented models in a membrane patch containing explicit homogenous POPC lipid molecules. The binding interaction between GRK1 and P* followed (83), with the understanding that GRK1 serves as a deactivating kinase for mammalian cone pigment (84). This was done by superimposing the opsin of the GRK1 complex (PDB ID code 7MTB) onto the membrane-embedded P* model. The structure of RDH8 (Uniprot no. Q9NYR8) was taken from the AlphaFold predicted

structural database (85). Three lipid-anchoring cysteine residues C298, C301, and C303 near the C terminus of RDH8 were palmitoylated using CHARMMGUI (82). Guided by these lipid anchors, RDH8 was manually positioned and oriented to depict its proximity to the membrane-embedded POps.

In Fig. 4*B*, the structure of PDE6 in complex with two $G_t\alpha$ subunits bound (PDB ID code 7JSN) was used as a blueprint to create models of singly or doubly activated PDE dimer complexes with zero, one, or two RGS9 molecules bound. The position and orientation of RGS9 molecules were obtained by superimposing the $G_t\alpha$–RGS9 complex (PDB ID code 1FQJ) onto the PDE6–$G_t\alpha$ complex over the $G_t\alpha$ region. CHARMMGUI was used to build the membrane patch with explicit homogenous POPC lipids.

Data, Materials, and Software Availability. All study data are included in the article and/or *SI Appendix*.

ACKNOWLEDGMENTS. This work was supported by National Eye Institute Grants U01EY032055 (to V.P.P. and R.S.), R01EY029710 (to V.P.P. and R.S.), U01EY025501 (to V.P.P. and R.S.), P30EY001730 (to V.P.P. and R.S.), and EY02660 (to E.N.P.); Research to Prevent Blindness Career Development Award (to V.P.P. and R.S.) and Unrestricted Grant (to the University of Washington Ophthalmology); the Foundation Fighting Blindness (V.P.P. and R.S.); and Burroughs Wellcome Fund Careers at the Scientific Interfaces Award (to R.S.). We thank Olaf Andersen, Marie Burns, Peter Calvert, Tom Glaser, Barry Knox, and Austin Roorda for helpful discussions and comments.

Author affiliations: [a]Ophthalmology, University of Washington, Seattle, WA 98109; [b]Physiology & Membrane Biology, University of California, Davis, CA 95616; and [c]Cell Biology & Human Anatomy, University of California, Davis, CA 95616

1. L. S. Lim, P. Mitchell, J. M. Seddon, F. G. Holz, T. Y. Wong, Age-related macular degeneration. *Lancet* **379**, 1728–1738 (2012).
2. P. T. de Jong, Age-related macular degeneration. *N. Engl. J. Med.* **355**, 1474–1485 (2006).
3. W. F. Drexler, *Optical Coherence Tomography* (Springer International, 2015).
4. J. G. H. Fujimoto, Foreword: 25 years of optical coherence tomography. *Invest. Ophthalmol. Vis. Sci.* **57**, 2 (2016).
5. A. Roorda, D. R. Williams, The arrangement of the three cone classes in the living human eye. *Nature* **397**, 520–522 (1999).
6. A. Roorda *et al.*, Adaptive optics scanning laser ophthalmoscopy. *Opt. Express* **10**, 405–412 (2002).
7. S. A. Burns, A. E. Elsner, K. A. Sapoznik, R. L. Warner, T. J. Gast, Adaptive optics imaging of the human retina. *Prog. Retin. Eye Res.* **68**, 1–30 (2019).
8. D. Hillmann *et al.*, In vivo optical imaging of physiological responses to photostimulation in human photoreceptors. *Proc. Natl. Acad. Sci. U.S.A.* **113**, 13138–13143 (2016).
9. M. Azimipour *et al.*, Optoretinogram: Optical measurement of human cone and rod photoreceptor responses to light. *Opt. Lett.* **45**, 4658–4661 (2020).
10. K. C. Boyle *et al.*, Mechanisms of light-induced deformations in photoreceptors. *Biophys. J.* **119**, 1481–1488 (2020).
11. V. P. Pandiyan *et al.*, The optoretinogram reveals the primary steps of phototransduction in the living human eye. *Sci. Adv.* **6**, eabc1124 (2020).
12. G. Ma, T. Son, T. H. Kim, X. Yao, Functional optoretinography: Concurrent OCT monitoring of intrinsic signal amplitude and phase dynamics in human photoreceptors. *Biomed. Opt. Express* **12**, 2661–2669 (2021).
13. R. F. Cooper, D. H. Brainard, J. I. W. Morgan, Optoretinography of individual human cone photoreceptors. *Opt. Express* **28**, 39326–39339 (2020).
14. F. Zhang, K. Kurokawa, A. Lassoued, J. A. Crowell, D. T. Miller, Cone photoreceptor classification in the living human eye from photostimulation-induced phase dynamics. *Proc. Natl. Acad. Sci. U.S.A.* **116**, 7951–7956 (2019).
15. A. Lassoued *et al.*, Cone photoreceptor dysfunction in retinitis pigmentosa revealed by optoretinography. *Proc. Natl. Acad. Sci. U.S.A.* **118**, e2107444118 (2021).
16. P. Zhang *et al.*, In vivo optophysiology reveals that G-protein activation triggers osmotic swelling and increased light scattering of rod photoreceptors. *Proc. Natl. Acad. Sci. U.S.A.* **114**, E2937–E2946 (2017).
17. U. Chawla *et al.*, Activation of the G-protein-coupled receptor rhodopsin by water. *Angew. Chem. Int. Ed. Engl.* **60**, 2288–2295 (2021).
18. R. S. Cantor, Lipid composition and the lateral pressure profile in bilayers. *Biophys. J.* **76**, 2625–2639 (1999).
19. M. Hollins, M. Alpern, Dark adaptation and visual pigment regeneration in human cones. *J. Gen. Physiol.* **62**, 430–447 (1973).
20. S. A. Burns, A. E. Elsner, L. A. Lobes Jr., B. H. Doft, A psychophysical technique for measuring cone photopigment bleaching. *Invest. Ophthalmol. Vis. Sci.* **28**, 711–717 (1987).
21. S. K. Shevell, Saturation in human cones. *Vision Res.* **17**, 427–434 (1977).
22. V. C. Smith, J. Pokorny, D. van Norren, Densitometric measurement of human cone photopigment kinetics. *Vision Res.* **23**, 517–524 (1983).
23. W. A. Rushton, G. H. Henry, Bleaching and regeneration of cone pigments in man. *Vision Res.* **8**, 617–631 (1968).
24. S. A. Burns, A. E. Elsner, Color matching at high illuminances: The color-match-area effect and photopigment bleaching. *J. Opt. Soc. Am. A* **2**, 698–704 (1985).
25. R. Sabesan, H. Hofer, A. Roorda, Characterizing the human cone photoreceptor mosaic via dynamic photopigment densitometry. *PLoS One* **10**, e0144891 (2015).
26. A. Meadway, L. C. Sincich, Light propagation and capture in cone photoreceptors. *Biomed. Opt. Express* **9**, 5543–5565 (2018).
27. J. M. Enoch, G. M. Hope, Directional sensitivity of the foveal and parafoveal retina. *Invest. Ophthalmol.* **12**, 497–503 (1973).
28. C. A. Curcio, K. R. Sloan, R. E. Kalina, A. E. Hendrickson, Human photoreceptor topography. *J. Comp. Neurol.* **292**, 497–523 (1990).
29. C. R. Chen, G. I. Makhatadze, ProteinVolume: Calculating molecular van der Waals and void volumes in proteins. *BMC Bioinformatics* **16**, 101 (2015).
30. L. D. Carter-Dawson, M. M. LaVail, Rods and cones in the mouse retina. I. Structural analysis using light and electron microscopy. *J. Comp. Neurol.* **188**, 245–262 (1979).
31. K. Palczewski, G protein-coupled receptor rhodopsin. *Annu. Rev. Biochem.* **75**, 743–767 (2006).
32. H. Imai, Y. Imamoto, T. Yoshizawa, Y. Shichida, Difference in molecular properties between chicken green and rhodopsin as related to the functional difference between cone and rod photoreceptor cells. *Biochemistry* **34**, 10525–10531 (1995).
33. G. P. Miljanich, L. A. Sklar, D. L. White, E. A. Dratz, Disaturated and dipolyunsaturated phospholipids in the bovine retinal rod outer segment disk membrane. *Biochim. Biophys. Acta* **552**, 294–306 (1979).
34. G. Wu, W. L. Hubbell, Phospholipid asymmetry and transmembrane diffusion in photoreceptor disc membranes. *Biochemistry* **32**, 879–888 (1993).
35. T. D. Lamb, E. N. Pugh Jr., Dark adaptation and the retinoid cycle of vision. *Prog. Retin. Eye Res.* **23**, 307–380 (2004).
36. M. H. Chen, C. Kuemmel, R. R. Birge, B. E. Knox, Rapid release of retinal from a cone visual pigment following photoactivation. *Biochemistry* **51**, 4117–4125 (2012).
37. Y. Imamoto, Y. Shichida, Cone visual pigments. *Biochim. Biophys. Acta* **1837**, 664–673 (2014).
38. P. Ala-Laurila *et al.*, Visual cycle: Dependence of retinol production and removal on photoproduct decay and cell morphology. *J. Gen. Physiol.* **128**, 153–169 (2006).
39. M. E. Estevez *et al.*, The 9-methyl group of retinal is essential for rapid Meta II decay and phototransduction quenching in red cones. *J. Gen. Physiol.* **134**, 137–150 (2009).
40. W. He, C. W. Cowan, T. G. Wensel, RGS9, a GTPase accelerator for phototransduction. *Neuron* **20**, 95–102 (1998).
41. E. R. Makino, J. W. Handy, T. Li, V. Y. Arshavsky, The GTPase activating factor for transducin in rod photoreceptors is the complex between RGS9 and type 5 G protein beta subunit. *Proc. Natl. Acad. Sci. U.S.A.* **96**, 1947–1952 (1999).
42. C. W. Cowan, R. N. Fariss, I. Sokal, K. Palczewski, T. G. Wensel, High expression levels in cones of RGS9, the predominant GTPase accelerating protein of rods. *Proc. Natl. Acad. Sci. U.S.A.* **95**, 5351–5356 (1998).
43. X. Zhang, T. G. Wensel, T. W. Kraft, GTPase regulators and photoresponses in cones of the eastern chipmunk. *J. Neurosci.* **23**, 1287–1297 (2003).
44. M. E. Burns, E. N. Pugh Jr., RGS9 concentration matters in rod phototransduction. *Biophys. J.* **97**, 1538–1547 (2009).
45. C. M. Krispel *et al.*, RGS expression rate-limits recovery of rod photoresponses. *Neuron* **51**, 409–416 (2006).
46. J. H. van Hateren, T. D. Lamb, The photocurrent response of human cones is fast and monophasic. *BMC Neurosci.* **7**, 34 (2006).
47. H. van Hateren, A cellular and molecular model of response kinetics and adaptation in primate cones and horizontal cells. *J. Vis.* **5**, 331–347 (2005).
48. S. C. Hsu, R. S. Molday, Glucose metabolism in photoreceptor outer segments. Its role in phototransduction and in NADPH-requiring reactions. *J. Biol. Chem.* **269**, 17954–17959 (1994).
49. S. C. Hsu, R. S. Molday, Glyceraldehyde-3-phosphate dehydrogenase is a major protein associated with the plasma membrane of retinal photoreceptor outer segments. *J. Biol. Chem.* **265**, 13308–13313 (1990).
50. A. R. Fersht, *Enzyme Structure and Mechanism* (W. H. Freeman, San Francisco, CA, 1977).
51. C. S. Pask, "Angular sensitivity of lens-photoreceptor systems" in *Photoreceptor Optics*, A. W. M. Snyder, Ed. (Springer Verlag, 1975), chap. A.8, pp. 159–174.
52. A. W. Snyder, C. Pask, The Stiles-Crawford effect–explanation and consequences. *Vision Res.* **13**, 1115–1137 (1973).
53. A. W. L. Snyder, *Optical Waveguide Theory* (Chapman & Hall, London, United Kingdom, 1983).
54. A. W. M. Snyder, *Photoreceptor Optics* (Springer-Verlag, New York, NY, 1975).
55. C. Friedburg, C. P. Allen, P. J. Mason, T. D. Lamb, Contribution of cone photoreceptors and post-receptoral mechanisms to the human photopic electroretinogram. *J. Physiol.* **556**, 819–834 (2004).
56. J. S. Kenkre, N. A. Moran, T. D. Lamb, O. A. Mahroo, Extremely rapid recovery of human cone circulating current at the extinction of bleaching exposures. *J. Physiol.* **567**, 95–112 (2005).
57. O. A. Mahroo, T. D. Lamb, Recovery of the human photopic electroretinogram after bleaching exposures: Estimation of pigment regeneration kinetics. *J. Physiol.* **554**, 417–437 (2004).
58. K. Sakurai, J. Chen, S. C. Khani, V. J. Kefalov, Regulation of mammalian cone phototransduction by recoverin and rhodopsin kinase. *J. Biol. Chem.* **290**, 9239–9250 (2015).
59. S. A. Vishnivetskiy *et al.*, Regulation of arrestin binding by rhodopsin phosphorylation level. *J. Biol. Chem.* **282**, 32075–32083 (2007).
60. Q. Liu *et al.*, The proteome of the mouse photoreceptor sensory cilium complex. *Mol. Cell. Proteomics* **6**, 1299–1317 (2007).
61. C. D. Lu *et al.*, Photoreceptor layer thickness changes during dark adaptation observed with ultrahigh-resolution optical coherence tomography. *Invest. Ophthalmol. Vis. Sci.* **58**, 4632–4643 (2017).
62. E. N. Pugh Jr., The discovery of the ability of rod photoreceptors to signal single photons. *J. Gen. Physiol.* **150**, 383–388 (2018).
63. T. J. Melia Jr., C. W. Cowan, J. K. Angleson, T. G. Wensel, A comparison of the efficiency of G protein activation by ligand-free and light-activated forms of rhodopsin. *Biophys. J.* **73**, 3182–3191 (1997).
64. T. E. Angel, S. Gupta, B. Jastrzebska, K. Palczewski, M. R. Chance, Structural waters define a functional channel mediating activation of the GPCR, rhodopsin. *Proc. Natl. Acad. Sci. U.S.A.* **106**, 14367–14372 (2009).
65. H. W. Choe *et al.*, Crystal structure of metarhodopsin II. *Nature* **471**, 651–655 (2011).
66. C. Chen, L. R. Blakeley, Y. Koutalos, Formation of all-trans retinol after visual pigment bleaching in mouse photoreceptors. *Invest. Ophthalmol. Vis. Sci.* **50**, 3589–3595 (2009).
67. J. D. Ding, R. Y. Salinas, V. Y. Arshavsky, Discs of mammalian rod photoreceptors form through the membrane evagination mechanism. *J. Cell Biol.* **211**, 495–502 (2015).

68. K. Mitra, I. Ubarretxena-Belandia, T. Taguchi, G. Warren, D. M. Engelman, Modulation of the bilayer thickness of exocytic pathway membranes by membrane proteins rather than cholesterol. *Proc. Natl. Acad. Sci. U.S.A.* **101**, 4083–4088 (2004).
69. V. Y. Arshavsky, T. G. Wensel, Timing is everything: GTPase regulation in phototransduction. *Invest. Ophthalmol. Vis. Sci.* **54**, 7725–7733 (2013).
70. M. Michaelides *et al.*, Novel mutations and electrophysiologic findings in RGS9- and R9AP-associated retinal dysfunction (Bradyopsia). *Ophthalmology* **117**, 120–127.e1 (2010).
71. K. M. Nishiguchi *et al.*, Defects in RGS9 or its anchor protein R9AP in patients with slow photoreceptor deactivation. *Nature* **427**, 75–78 (2004).
72. R. Sharma *et al.*, Formation and clearance of all-trans-retinol in rods investigated in the living primate eye with two-photon ophthalmoscopy. *Invest. Ophthalmol. Vis. Sci.* **58**, 604–613 (2017).
73. R. Sharma *et al.*, In vivo two-photon fluorescence kinetics of primate rods and cones. *Invest. Ophthalmol. Vis. Sci.* **57**, 647–657 (2016).
74. V. P. Pandiyan *et al.*, High-speed adaptive optics line-scan OCT for cellular-resolution optoretinography. *Biomed. Opt. Express* **11**, 5274–5296 (2020).
75. S. B. R. Stevenson, A. Roorda, Correcting for miniature eye movements in high resolution scanning laser ophthalmoscopy. *Proc. SPIE* **5688**, 6 (2005).
76. X. Jiang, J. A. Kuchenbecker, P. Touch, R. Sabesan, Measuring and compensating for ocular longitudinal chromatic aberration. *Optica* **6**, 981–990 (2019).
77. J. I. Morgan, E. N. Pugh Jr., Scanning laser ophthalmoscope measurement of local fundus reflectance and autofluorescence changes arising from rhodopsin bleaching and regeneration. *Invest. Ophthalmol. Vis. Sci.* **54**, 2048–2059 (2013).
78. P. Zhang, M. Goswami, R. J. Zawadzki, E. N. Pugh Jr., The photosensitivity of rhodopsin bleaching and light-induced increases of fundus reflectance in mice measured in vivo with scanning laser ophthalmoscopy. *Invest. Ophthalmol. Vis. Sci.* **57**, 3650–3664 (2016).
79. G. Westheimer, The Maxwellian view. *Vision Res.* **6**, 669–682 (1966).
80. Y. Song *et al.*, High-resolution comparative modeling with RosettaCM. *Structure* **21**, 1735–1742 (2013).
81. A. L. Lomize, I. D. Pogozheva, H. I. Mosberg, Anisotropic solvent model of the lipid bilayer. 2. Energetics of insertion of small molecules, peptides, and proteins in membranes. *J. Chem. Inf. Model.* **51**, 930–946 (2011).
82. E. L. Wu *et al.*, CHARMM-GUI Membrane Builder toward realistic biological membrane simulations. *J. Comput. Chem.* **35**, 1997–2004 (2014).
83. Q. Chen *et al.*, Structures of rhodopsin in complex with G-protein-coupled receptor kinase 1. *Nature* **595**, 600–605 (2021).
84. A. L. Lyubarsky, C. Chen, M. I. Simon, E. N. Pugh Jr., Mice lacking G-protein receptor kinase 1 have profoundly slowed recovery of cone-driven retinal responses. *J. Neurosci.* **20**, 2209–2217 (2000).
85. M. Varadi *et al.*, AlphaFold Protein Structure Database: Massively expanding the structural coverage of protein-sequence space with high-accuracy models. *Nucleic Acids Res.* **50**, D439–D444 (2021).
86. S. A. Schädel *et al.*, Ligand channeling within a G-protein-coupled receptor. The entry and exit of retinals in native opsin. *J. Biol. Chem.* **278**, 24896–24903 (2003).
87. P. A. Liebman, Microspectrophotometry of retinal cells. *Ann. N. Y. Acad. Sci.* **157**, 14 (1969).